JOURNAL OF AIRCRAFT
Vol. 44, No. 5, September–October 2007

Analysis and Design of Robust Helium Aerostats

Jonathan I. Miller* and Meyer Nahon†
McGill University, Montreal, Quebec H3A 2K6, Canada

DOI: 10.2514/1.25627

Tethered helium aerostats are receiving renewed attention in the scientific and surveillance communities. However, conventional aerostats cannot consistently survive high winds. The goal of this research was to design an aerostat that could be deployed for very long periods, thus reducing operating costs and interruptions in data acquisition. Existing designs and fabrication techniques were first reviewed and replicated in the construction of a 2.5-m-diam spherical aerostat. The constructed balloon was then flown outdoors to observe its operational qualities. The results from the flights were used to inform finite element models evaluating the critical stresses in the envelopes of 10.15-m-diam balloons with two different tether attachment schemes. The models suggested that conventional aerostats would fail in high winds, due to stress concentrations where the tethers meet the envelope. A third model was created to appraise the performance of an ultrarobust aerostat with a partial-hard carbon fiber shell in critical areas, which was able to achieve an operational safety factor of 1.6 in a 46.3-m/s (90-kt) wind.

I. Introduction

THE tethered helium aerostat is an old concept that is being revitalized, due to the advent of new materials and applications. A typical tethered aerostat system consists of a fabric envelope to contain the lifting gas, one or more tethers to moor the balloon to the ground, a flying harness to distribute the tether load over the aerostat, load patches to attach the flying harness to the envelope, and occasionally, a pressure-regulation system known as a ballonet.

Aerostats are commonly used for positioning aerial platforms for environmental, astrophysical, communications, and surveillance applications. Examples include the Tethered Aerostat Radar System (TARS), which is a large aerostat-based border surveillance system being used in the southern United States, and the Rapid Aerostat Initial Deployment (RAID) system prototype, which was used for military surveillance in Afghanistan [1]. In many of these applications, it is critical (with respect to maintaining a constant stream of data acquisition, as well as minimizing the operating costs) that the balloon remain aloft for long durations of time. Yet the airborne time of today's typical tethered aerostat system is "generally limited by weather" [1]. The balloons are not reliably able to survive high winds, due to "dimpling" (a loss in envelope shape caused by high surface pressures) and due to the point loads produced where the mooring lines attach to the envelope. The use of synthetic materials and laminates with high strength-to-weight ratios has improved the survivability and reliability of modern aerostats [2]. To create a near-perpetually deployed aerostat, however, other changes, such as the use of an ultrarobust envelope partially made from a hard material, must be investigated. Such an investigation requires knowledge of the conventional materials and construction techniques used to build tethered balloons, the dynamics of the buoyant bodies, and how the stresses from the tether loads are distributed over the envelope. The research discussed here was performed on spherically shaped aerostats. Although they have a higher drag coefficient than their blimp-shaped, streamlined counterparts, they also cost less and are simpler to manufacture and operate, are subject to lower hoop stresses, and do not require a special ground-mooring apparatus to allow weathervaning [2].

Received 27 June 2006; revision received 8 May 2007; accepted for publication 15 May 2007.

*Research Assistant, Department of Mechanical Engineering, 817 Sherbrooke Street West.

†Associate Professor, Department of Mechanical Engineering, 817 Sherbrooke Street West. Associate Fellow AIAA.

Tethered aerostat systems have received limited attention in recent literature, and that work has predominantly focused on the dynamics of streamlined aerostats. The techniques used for fabricating gas balloons have changed little over the last century, however, and the 1926 work by Upson [3] remains a key reference for the design and construction of envelopes and mooring structures. In 1997 and 1998, Recks [4,5] provided very thorough and more modern guides to building small helium blimps. These guides contain a wealth of information about envelope materials, plotting two-dimensional gores, and assembly procedures that can be extended to the domain of spherical aerostats. More recently, in 1999, Khoury and Gillett [2] wrote a comprehensive review of numerous aspects of airship design, including higher-level information on the materials and bonding procedures that are used in classical and modern airship envelopes and that are also applicable to aerostat construction.

On the topic of the dynamics of tethered buoyant spheres, Williamson and Govardhan [6–8] performed the most relevant body of work. They found that the spheres would not maintain a constant inclination angle in a stream flow, but would tend to oscillate in a characteristic figure-eight motion. They reported that the oscillation amplitudes were dependent on the flow speed and that the drag coefficients of the spheres were up to 100% higher than those for smooth fixed spheres. Govardhan and Williamson [7] also went on to investigate the influence of vortex shedding in exciting tethered spheres of differing sizes and tether lengths. They found that there was a resonance when the stationary shedding frequency coincided with the natural pendulum frequency of the tethered systems, known as the *lock-in* phenomenon. They later found high-speed modes of tethered-sphere vibrations occurring at stream speeds higher than can be explained by classical lock-in, and they speculated that a motion-induced force must have been exciting the tethered spheres' oscillation frequencies [8].

The only study found of the hull stresses on a tethered aerostat in flight was performed in 1982 by Hunt [9] for TCOM. Hunt used NASTRAN to evaluate the stress contours over TCOM's larger aerostats subjected to different internal pressures, gravitational forces, and experimentally determined aerodynamic pressures for a range of wind speeds from 0–46.3 m/s (0–90 kt). He found that the highest stresses were at the maximum diameter of the balloon and the load patches. The analysis was limited, though, as it considered only small deflections and used a coarse mesh, constrained by the computational power available, that did not allow for detailed stress concentration results. Hunt [10] performed a second finite element stress analysis in 1993 to determine the survivability of a lightweight nose structure for mooring an aerostat in high winds. The analysis demonstrated that the structure could withstand 46.3-m/s (90-kt) winds with the appropriate safety factor, but it provided little information about the stresses in the hull.

Baginski and Collier [11] used energy methods in 2001 to perform finite element analyses, looking at the stresses in the envelopes of large high-altitude free balloons constrained by their launching spool. Baginski and Schur [12] extended this analysis in 2003 with a parametric study to structurally optimize the shapes of these specialized balloons. The analyses gave good insight into how to model thin-walled buoyant pressure vessels, but did not look into the stress contours or failure methods of conventional tethered aerostats specifically. As for the finite element analyses of related tethered-fabric systems or lighter-than-air systems such as parachutes, sails, and airships, the available studies did not focus on detailed stress contours and were not appropriate to the task of evaluating aerostat failure.

In 1980, Durney [13] outlined the causes of local failure in large aerostat envelopes. He devised a means of preventing the propagation of local failures into catastrophic failures by installing a network of high-strength rip-stop material, thereby reducing damage and repair costs, but did not look into preventing local failures in the first place.

The research described here was directed at extending the limited studies published by Hunt [9,10] on the mechanisms of tethered-aerostat failure in flight and investigating alternative concepts for the design of a robust tethered spherical balloon capable of withstanding high winds for long periods of time. As a first step, existing construction and design techniques were reviewed and replicated by building a small spherical balloon. The constructed balloon was then flown outdoors at different altitudes to study its drag coefficient and oscillatory behavior in various natural wind conditions. The results of the flights were used to inform NASTRAN-based finite element models of two separate balloons, which determined the critical stresses in the envelope when using two different tether attachment methods. A novel ultrarobust aerostat with a partial-hard shell made of carbon fiber in critical areas was then designed, and a corresponding finite element analysis model was assembled to evaluate the structural performance of this partial-hard aerostat against the fully fabric models.

II. Construction and Flight of a Small Helium Aerostat

A. Construction of a Small Fabric Balloon

To achieve a good compromise between cost, ease of storage and handling, and a usable product, it was decided to construct the smallest balloon possible that would stay aloft in a 10-m/s wind. It was determined that the aerostat should have at least 44.1 N (4.5 kg) of net static lift when considering only the weight of the helium and envelope in the lift calculation. It was also decided that the material employed in the envelope had to be commonly found in industrial aerostat envelopes and not require the use of special equipment for construction of the balloon.

Lamcotec was chosen as the optimum supplier for the envelope fabric because of their experience dealing with amateur and professional balloonists. Lamcotec's 142-g/m^2 (4.2-oz/yd^2) single-coated heat-sealable no. 109 70-denier urethane-coated nylon taffeta was selected because it was the lightest helium-impermeable material available that could be easily manipulated. Knowing the weight of the material to be used, the minimum radius of the aerostat needed to meet the lift requirement of 44.1 N at sea level and 25°C was determined to be 1.19 m. A radius of 1.25 m was chosen for the aerostat, which would produce a net lift of 53.2 N.

The most common methods of securing the tethers to the envelope are through load patches (large patches of material bonded to the side of the envelope), straps that start at the top of the balloon and run down its perimeter, or through a net draped over the top of the of the aerostat (Fig. 1). Though it is the heaviest approach, using a net was deemed most appropriate, because it best distributes load and is easiest to implement. Qued Seaway Plastics Ltd.'s 2-180B untreated 44-mm-mesh natural nylon netting was selected for the net, because it is strong and light, with a specific weight of 170 g/m^2. The size of the net was chosen to cover the balloon down to 35 deg below its equator so that the tethers would attach to the tangent of the balloon at that point and make a 35-deg angle with the vertical, as recommended by Upson [3]. The entire net weighed 24.6 N, which reduced the lift of the balloon from 53.2 to 28.6 N.

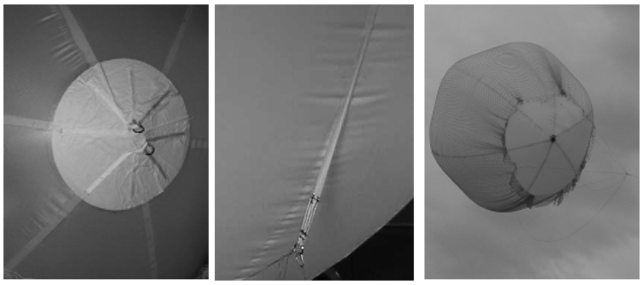

Fig. 1 Tether-attachment methods.

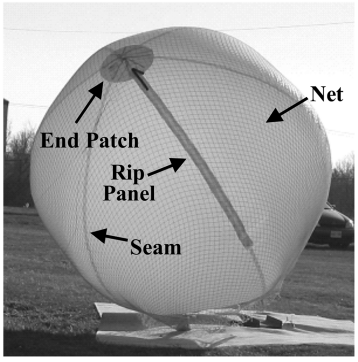

Fig. 2 Finished balloon.

A six-gore configuration was chosen for the aerostat, the minimum used in the industry to maintain a spherical shape. To assemble the aerostat, the gores were first traced onto sheets of urethane-coated nylon with the aid of a modified Smalley chart [14]. They were then cut out with ordinary scissors and heat-sealed urethane to urethane using a Teflon-coated hobby iron at 175°C, creating a 25-mm seam. An end patch and filler valve were bonded to the balloon using vinyl cement to seal off the ends. With the balloon built, a rip panel was installed in the envelope to induce a controlled descent in case of an emergency. The rip panel, shown in Fig. 2 as part of the finished balloon, consisted of a large slit in the envelope that started at the top of the balloon and ran one-fifth of the circumference down, covered by a reinforced piece of fabric that is opened to rapidly deflate the balloon in the event of an emergency [3].

B. Flight Dynamics of the Tethered Spherical Aerostat

The 2.5-m-diam spherical aerostat was flown outdoors at tether lengths of 15, 30, and 45 m, while moored to the ground by a single tether, to evaluate its motion characteristics and drag coefficient. The load in the main tether of the balloon was recorded with a load cell, and the wind speed and direction were recorded with wind monitors. The three-dimensional position of the balloon relative to the winch was measured with a low-cost differential GPS system that consisted of a roving remote station receiver attached to the top of the balloon along the axis of the tether and a static base station receiver placed at a known fixed location on the ground, as shown in Fig. 3. The lift of the aerostat was also measured at the start of each day of testing.

Williamson and Govardhan [6] observed that a buoyant tethered sphere in a steady stream flow will tend to oscillate both inline and transverse to the flow, rather than maintain a steady inclination angle, and the combination of these two oscillations produces a figure-eight motion. Our 2.5-m aerostat did oscillate in a direction transverse to the stream flow (Fig. 4), but due to varying wind conditions caused by gusts, it did not exhibit a discernible figure-eight pattern. More details on the test conditions and data collected can be found in [15].

If the motion of the balloon is averaged over several periods of oscillation, the inertial terms due to the balloon accelerations will

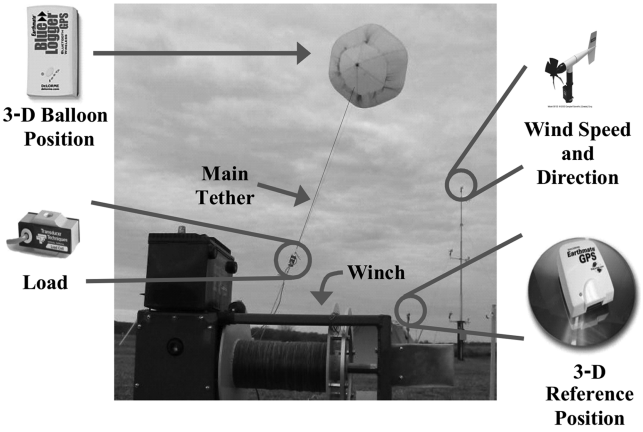

Fig. 3 Experimental setup.

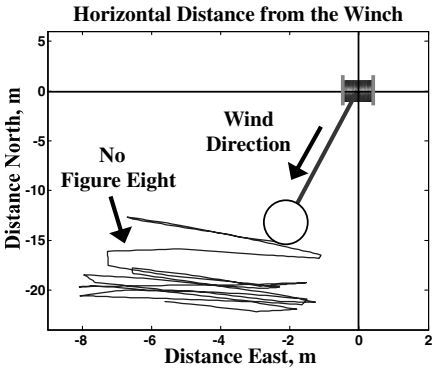

Fig. 4 Motion of the aerostat during a typical 30-m flight.

average to zero and a quasi-static state may be assumed. Using the quasi-static assumption, the drag force on the tethered sphere, F_D, was determined from its average observed inclination angle, herein referred to as the blowdown angle, and from the known lift force. The drag coefficient of the tethered sphere, $\bar{C}_D$, was then calculated with

$$\bar{C}_D = \frac{\bar{F}_D}{\frac{1}{2}\rho_{\text{air}}\bar{u}^2\pi r^2} \tag{1}$$

where r is the radius of the balloon, ρ_{air} is the density of the surrounding air, $\bar{u}$ is the mean wind speed that the sphere is subjected to, and the overbar indicates averaging over several periods.

The Reynolds number range investigated was 2.8×10^5–8.2×10^5. Taking into account the surface roughness caused by the net, the flow was considered to be supercritical in this range [15,16]. An average drag coefficient of 0.88 was calculated for the aerostat, much higher than the value of 0.15 for a smooth fixed sphere in supercritical flow and higher than the value of 0.7 found by Govardhan and Williamson [7] for smooth tethered spheres in subcritical flow. A possible reason for the high drag coefficient of the 2.5-m balloon is that the aerostat was not perfectly spherical, due to the use of only six gores, giving it a less streamlined hexagonal shape. Because of offsets and inaccuracies in the GPS system used, the drag coefficient found is tentative at best. The existence of higher drag coefficients for buoyant tethered spheres when compared with fixed smooth spheres, however, will prove to be key knowledge for the analysis of the stresses seen in the balloon's envelope during flight.

III. Finite Element Analysis of a Fabric Aerostat

The catastrophic failure of aerostats in high winds tends to occur when a local failure of the envelope propagates into a massive tear [13]. To quantify exactly how and why aerostats fail, a finite element analysis of the stresses in the envelope was conducted to see where stress concentrations exist and what limits fabric aerostats from operating in high wind speeds. NASTRAN was used for the simulations, and a nonlinear static analysis of the envelope was performed, because it was expected that the envelope deflection would be large [17]. The analysis assumed a quasi-static state for the balloon, with the inertial terms being equal to zero.

A. Finite Element Model

Two different kinds of aerostats were analyzed: one in which the tethers attached to the envelope through load patches and one in which they attached through straps. The 2.5-m aerostat described previously is not very suitable for carrying practical payloads, and so the investigation was performed on larger (10.15-m-diam) aerostats, the size being considered for the National Research Council of Canada's (NRC's) one-third-scale large adaptive reflector experiment [18]. The ballonets and seams were omitted for simplicity, due to their lack of influence on the major hull stresses.

The first model (Fig. 5a) featured eight tethers that each separated into eight subtethers before attaching to the tangent of the balloon through 500-mm-diam load patches spaced at equal intervals around a ring 35 deg below the equator of the sphere. Point attachments were simulated by tying the end nodes of the subtethers to nodes on the load patch. The tethers and subtethers were modeled as cylinders of 11 and 15 mm in diameter, respectively, the appropriate diameters for a balloon of this size [15]. The load patches were simulated as circular areas of the envelope in which the thickness doubles, which assumes a perfect bond between the two. Further details about the model can be found in [15].

The second model (Fig. 5b) featured eight tethers that each attached to the tangent of the balloon through 25-mm-wide, 3-mm-thick straps. The straps were sewn directly into the envelope, ran over the top of the balloon, and separated from the envelope 32 deg below

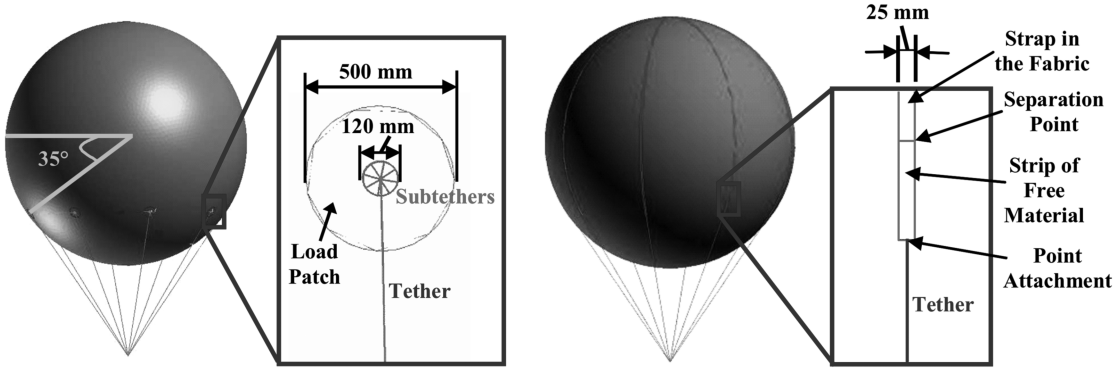

a) Model featuring load patches b) Model featuring straps

Fig. 5 Models of the 10.15-m-diam aerostats.

Table 1 Material properties

Nylon 6 [19]				Cortland plasma rope			
Young's modulus	2.5 GPa	Thickness	0.18 mm	Young's modulus	37.4 GPa	Subtether diameter (load patch)	15 mm
Poisson's ratio	0.39	Areal Density	205 g/m^2	Density	980 kg/m^3	Tether break strength	93.4 kN
Density	1140 kg/m^3	Break strength	142 MPa	Tether diameter	11 mm	Subtether break strength (load patch)	169 kN

the equator of the sphere. The straps, similar to the load patches, were simulated as extra-thick sections of the envelope, thus assuming a perfect bond between the two. Attached to the end of each strap was a 25-mm-wide, 3-mm-thick strip of free material that connected to the tethers 35 deg below the equator of the balloon. The connections between the ends of the strips of free material and the tethers were approximated by tying nodes together between the two.

Both 10.15-m-diam balloons were made from Lamcotec's 205-g/m^2 (6.05-oz/yd^2) urethane-coated nylon. In the absence of detailed orthotropic mechanical properties for this laminate, the envelope material was approximated as being linear elastic isotropic nylon 6, used as the load-bearing component of some airship envelope materials [2], but with the thickness, areal density, and break strength of the Lamcotec fabric. The approximation of isotropy is commonly made when performing finite element analyses of fabric inflatables [11,12]. The tethers were made of Cortland's plasma 12-strand rope and were also approximated as being linear elastic isotropic. The properties of the envelope and tether materials are shown in Table 1.

The envelope of both models was made from linear triangular elements, because these elements conform better to curved boundaries than linear rectangular elements and have reduced computational needs over those of quadratic triangular elements [20]. To avoid instabilities in the equations used by NASTRAN for the nonlinear analysis, beam and shell elements with small bending stiffnesses on the order of 1% of the tensile stiffness had to be used for the envelope and tethers, respectively. Both balloon models were split up into approximately 18,000 mesh elements, with the density of the finite element meshes chosen to obtain a balance between accuracy of the results and low computational time.

A tethered aerostat is a marginally constrained structure, and as a result, it was found that fixing the finite element models only at the confluence point of the tethers led to singularities in the stiffness matrices that caused diverging displacements to be generated by NASTRAN. The next most realistic solution for the model with load patches was to constrain each tether, but not the subtethers, in its entirety from translating in any direction. This is equivalent to having infinitely stiff tethers. For the model with straps, both the tethers and the free strips of material at the ends of the straps had to be constrained from translating in any direction. Because the main interest of the analysis was the stress distribution in the envelopes of the balloons, these approximations were deemed acceptable.

B. Simulated Loads

The forces applied to the models included aerodynamic and internal pressure distributions and gravity. The drag-causing static pressure distribution over a tethered buoyant sphere as it moves through the air is not available in literature, and the aerodynamic load was approximated using the distribution over a smooth *fixed* sphere in high Reynolds number steady flow. The highest Reynolds number for which this static pressure distribution is available was published by Achenbach [21] for $Re = 50.0 \times 10^5$ and is shown in Fig. 6. It is of interest to analyze envelope stresses at high wind speeds, and a Reynolds number of this magnitude corresponds to a relatively low 7.1-m/s wind speed for a 10.15-m-diam spherical aerostat. As seen in Fig. 6, however, the static pressure profile does not change dramatically for high Reynolds numbers, because the separation point of the flow from the sphere remains relatively constant. It was therefore deemed reasonable to use this distribution for higher Reynolds numbers. A further issue with using the depicted distribution is that it implies a drag coefficient of only 0.23. As discussed in Sec. II, the drag coefficient of tethered buoyant spheres tends to be much higher than this, an issue that will be addressed later.

Helium has a lower density than air, and its pressure decreases more slowly over a change in height z. Referring to the balloon in Fig. 7, if the pressures of the two gases are equal at some reference height z_o, a differential pressure will act outward to the envelope above that height, with the resultant being an upward buoyant force. It follows that buoyancy was simulated in the program by varying the internal pressure of the balloons, p_i, as

$$p_i = \bar{p}_i + (\rho_{\text{air}} - \rho_{\text{he}}) g z_e \tag{2}$$

where ρ_{he} is the density of helium; g is the gravitational acceleration of 9.81 m/s^2; $\bar{p}_i$ is the mean internal overpressure for the balloon, taken to be 249 Pa (1 inWG); and z_e is the vertical distance in meters from the center of the balloon. Integrating the pressure profile described by Eq. (2) over the surface of a 10.15-m aerostat yields a gross lift of 5.62 kN. With gravity simulated as an acceleration equal to g and applied to the entire model, taking into account the weight of the envelope and enclosed helium, the net lift of the aerostat was determined by NASTRAN to be 4.97 kN.

The highest wind speed at which the models can be evaluated is constrained by dimpling, or a loss of the aerostat's spherical shape when the dynamic pressure of the wind exceeds the internal pressure of the balloon. Dimpling will first occur at the stagnation point because, referring to Fig. 6, the aerodynamic pressure has its highest positive value there. Once a dimple is formed, the balloon turns into more of a sail, causing the drag forces to rise as the entire dimpled area is exposed to the stagnation pressure, rendering the assumed static pressure distribution invalid. Because the stagnation point will

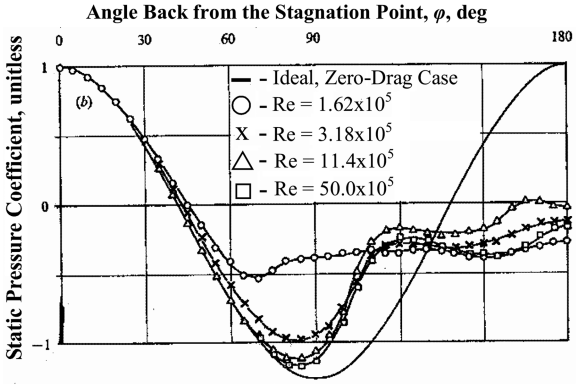

Fig. 6 Static pressure distribution over a smooth fixed sphere [21].

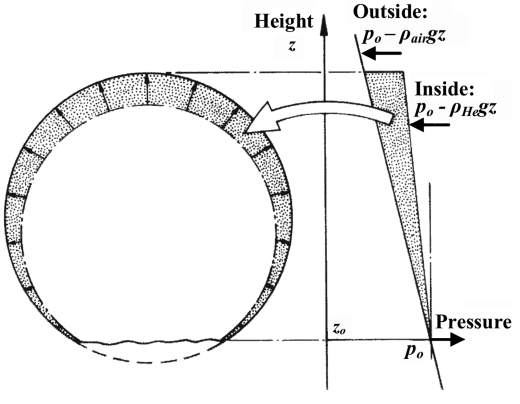

Fig. 7 Mechanism of buoyant lift [2].

always be at the center of the balloon, where $p_i = 249$ Pa, dimpling occurs when $1/2\rho_{\text{air}}u^2 > 249$ Pa, or when $u > 20$ m/s, corresponding to a Reynolds number of 141×10^5 for a 10.15-m-diam spherical aerostat.

C. Results of the Finite Element Analysis for the Balloon with Load Patches

Away from the influence of the tether attachment points, the stress in the envelope of the aerostat, σ_E, is mainly a hoop stress, described by

$$\sigma_E = \frac{(p_i - p_a)r}{2t} \tag{3}$$

where t is the thickness of the envelope membrane material, and p_a is the aerodynamic pressure. The hoop stress in the envelope at the point that is diametrically opposite the stagnation point, far from the influence of the tethers, was calculated with Eq. (3) to be 4.10 MPa at the dimple speed. The hoop stress returned by NASTRAN at that point for the aerostat with load patches was within 0.5% of the expected value. Similar accuracies for the hoop stress were found for all wind speeds evaluated. Moreover, the simulated constraint force in the tethers was within 0.8% of analytically calculated values, supporting the validity of the model.

The distribution of the stresses over the envelope of the aerostat equipped with load patches for six different wind speeds from 0 m/s to the dimple speed is shown in Fig. 8. Those areas in which a mesh is seen represent regions in which the deformed shape of the aerostat is internal to the original shape. Because Eq. (3) is proportional to the net pressure on the fabric, as the wind speed rises and the aerodynamic pressure begins to dominate the internal pressure, the aerodynamic pressure has an increasing influence on the stresses in the envelope. This causes the distribution of the stresses over the aerostat to increasingly resemble the pressure distribution depicted in Fig. 6. For all wind speeds, the envelope stresses are approximately 1.5 MPa higher at the top of the aerostat than at the bottom, due to the internal pressure rising by 104 Pa over the height of the envelope.

A more detailed illustration of the stresses over the aerostat when subjected to the limiting wind speed of 20 m/s is shown in Fig. 9a. We see that there are large membrane stresses of up to 9.7 MPa at the top of the balloon, 80 deg back from the stagnation point. Figure 6 shows that the aerodynamic pressure of highest magnitude occurs approximately 80 deg from the stagnation point and is due to a suction on the surface. The high aerodynamic suction combines with the large internal pressure at the top of the balloon to create this region of large skin stress.

The highest stresses in the envelope were concentrated around the load patches. The net drag (which is primarily due to the separated region at the rear of the sphere) and buoyancy caused the balloon to "tug" on the constraining tethers, loading the tethers and creating high stresses where they attach to the envelope. These tensile stresses were concentrated just above the load patch, a consequence of the membrane thickness halving when moving from the load patch to the envelope. However, due to the variable membrane stresses caused by the different aerodynamic pressures over the balloon, these concentrations were not even among all eight patches. The maximum stress, equal to 19.9 MPa, occurred at the lower load patch on the side of the balloon in Fig. 9a, located approximately 75–80 deg back from the stagnation point in the region of high aerodynamic pressure. The material in this region had a higher membrane stress before the stress concentration from the constraining tethers was considered, which increased the magnitude of the total combined stress as a result.

The lowest stresses in the envelope, around 1.02 MPa, are in the region of the stagnation point. This is because at the near-dimpling wind speed of 20 m/s, the aerodynamic pressure is equal in magnitude and opposite in sense to the internal pressure, and so they cancel each other out. The region of the stagnation point also displaces back slightly farther than those areas around it (about

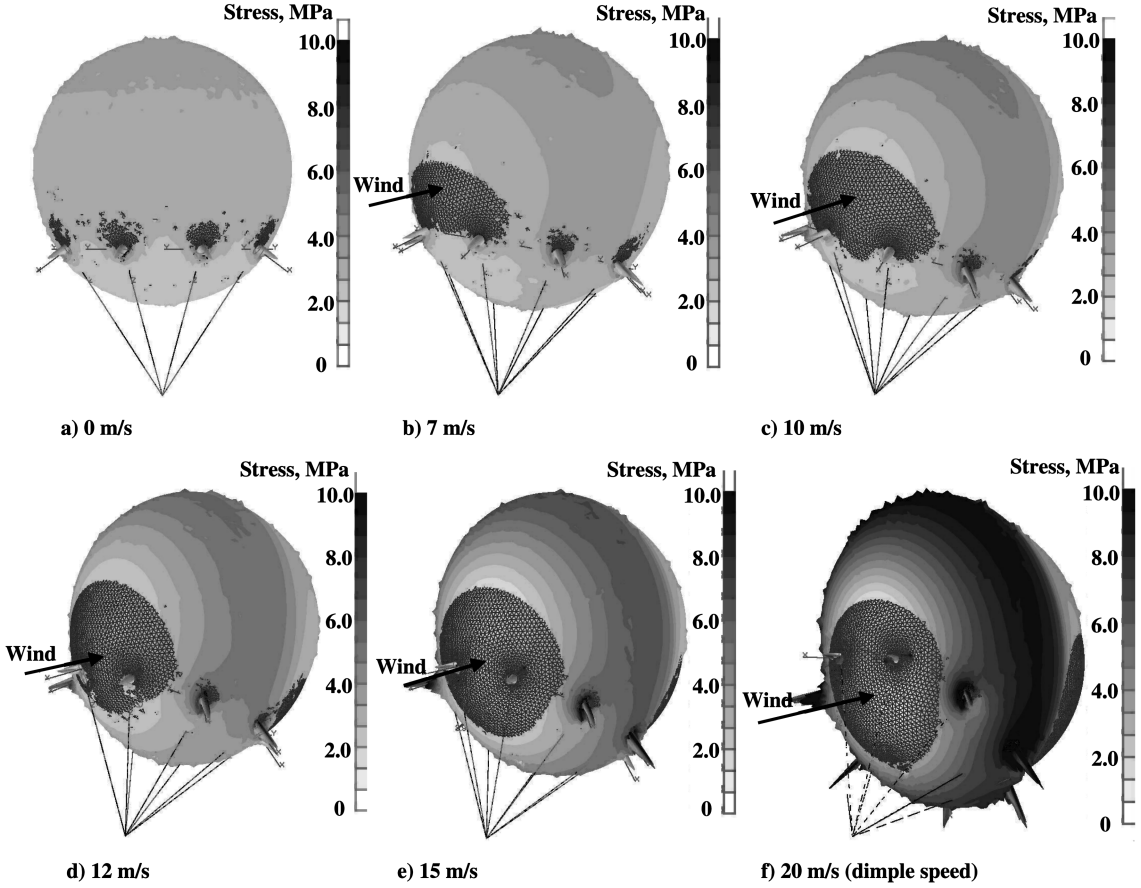

Fig. 8 Stress profiles over the fabric aerostat equipped with load patches subjected to different wind speeds (exaggerated displacements, range narrowed to 0–10 MPa for all plots).

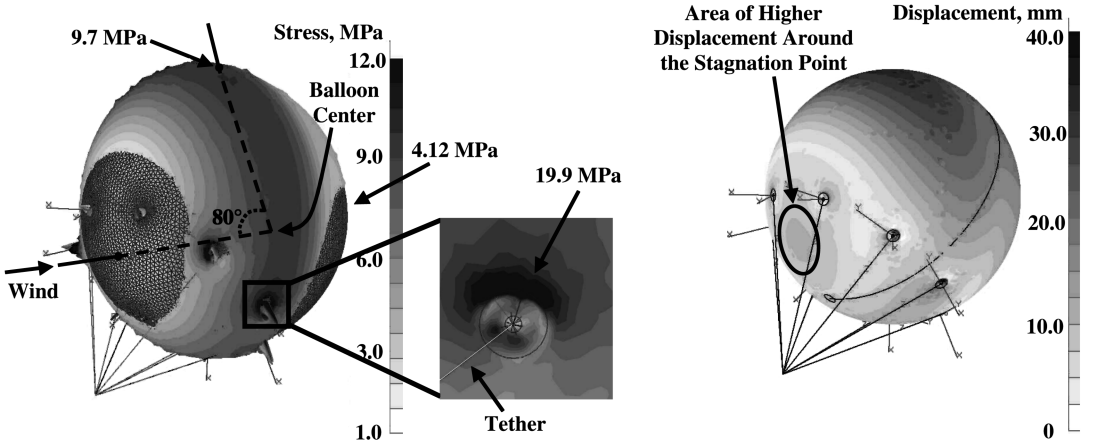

a) Stresses (exaggerated displacements) b) Displacements (unexaggerated displacements)

Fig. 9 Stress and deformation profiles over the fabric aerostat with load patches in a 20-m/s wind.

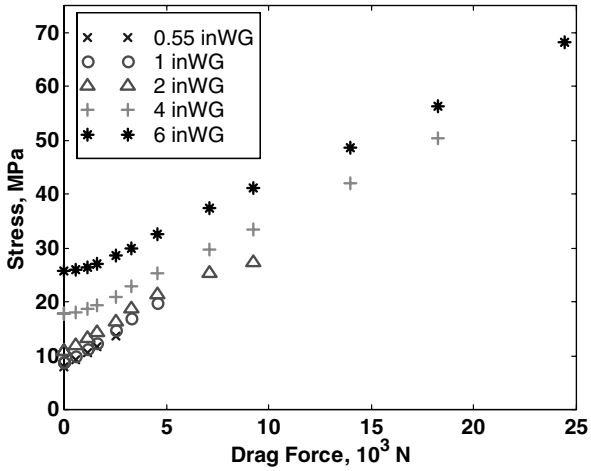

Fig. 10 Rise in maximum envelope stress with drag force and internal pressure.

12 mm, compared with 7 mm, illustrated in Fig. 9b), indicating the onset of dimple. The displacements over the entire envelope of the balloon shown in Fig. 9b will cause its shape to digress slightly from being spherical, changing the static pressure distribution. However, the maximum displacement seen was 56 mm, which was considered negligible with respect to the overall size of the aerostat.

It will be shown shortly that at higher wind speeds, the largest stresses in the balloon, the stress concentrations near the load patches, are caused predominantly by aerodynamic effects. The aerodynamic effects depend on the pressure distribution over the aerostat, which is described by the drag coefficient, and on the dynamic pressure of the wind. Because both of these quantities can vary, it is desirable to analyze changes in envelope stress with drag force, which encompasses the contributions of the two variables.

The simulation was run for several different combinations of internal pressure and wind speed to see the effect of internal pressure and drag force on the maximum stresses. For each internal pressure, the maximum wind speed simulated was the dimple speed at that pressure. The maximum stress for each test case is plotted against drag force in Fig. 10. A linear relationship was found between the maximum envelope stress and the drag force for higher values of drag, and consequently for higher wind speeds, but the relationship was not exactly linear for wind speeds below 12 m/s ($F_D = 1.64$ kN) and internal pressures above 498 Pa (2 inWG). At these lower wind speeds, the invariant lift force ($F_L = 4.97$ kN) is more than triple the drag force, and thus has a greater influence on the envelope stresses. Because the base membrane stress increases with rising internal pressure, the effect of the lift dominating the drag is more pronounced at higher internal pressures.

D. Results of the Finite Element Analysis for the Balloon with Straps

The simulation of the aerostat equipped with straps was run for several different wind speeds from 0 m/s to the dimple speed of 20 m/s. The model was validated by cross-referencing simulated hoop stresses and constraint forces with analytically calculated values. The results were accurate to within 2% for all wind speeds. The distribution of the stresses over most of the envelope of the aerostat with straps was very similar to that of the balloon with load patches for all wind speeds. However, it is interesting to observe what happened around the straps.

As wind speeds rise, the aerostat "tugs" harder on the constraining tethers, and it is logical to expect that the straps would be increasingly loaded. Figure 11a shows, however, that at the dimple speed, the stresses in and around the straps are counterintuitively much lower than the stresses in the surrounding envelope. This is because the straps are sewn directly to the fabric envelope and cannot move relative to it. The lack of relative movement forces part of the load and associated stresses to concentrate in the envelope in the region in which the straps separate from the fabric sphere, yielding stresses of up to 15.4 MPa in a 20-m/s wind. This same concentration pattern was observed during experiments with an off-the-shelf balloon equipped with straps, as seen in Fig. 11b.

A comparison of the maximum stresses in the aerostats with straps and load patches is shown in Fig. 12. The stresses in the balloon equipped with straps exhibited a linear relationship with drag force, similar to the balloon with load patches, demonstrating that this relationship is independent of the tether attachment method. The stresses around the tether attachment points in the balloon with straps were approximately 3.8 MPa lower than those in the balloon with load patches for all drag forces (and consequently for all wind speeds), and the stresses in the former were mainly due to shear, whereas the stresses in the latter were tensile. The lower stresses in the balloon with straps indicate that this attachment method better alleviates stress concentrations, by undertaking some of the tensile load and more thoroughly distributing the remaining load over the envelope.

E. Practical Considerations and Extra Comments

There are two important assumptions made in the preceding analyses. The first is the relatively low drag coefficient of 0.23 for the aerostat. Previous literature and the experiments in Sec. II indicate that the drag on a tethered free sphere is much higher than this [7]. The flowfield around and behind a tethered sphere as it moves is more complex and turbulent than the flowfield behind a fixed sphere, creating more drag and consequently raising the tether loads. The drag coefficient presented in Sec. II for the 2.5-m aerostat was considered too inaccurate for the present analysis and, consequently, a coefficient had to be taken from the literature. Govardhan and Williamson [7] published the only experimental drag coefficient data

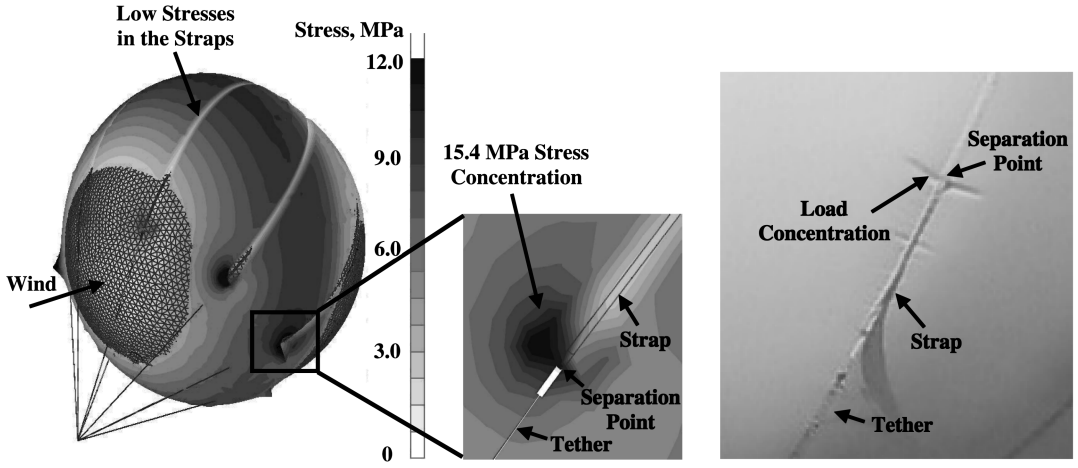

a) Stresses in a 20 m/s wind (exaggerated displacements) b) Observed load concentrations

Fig. 11 Stresses in the fabric aerostat equipped with straps.

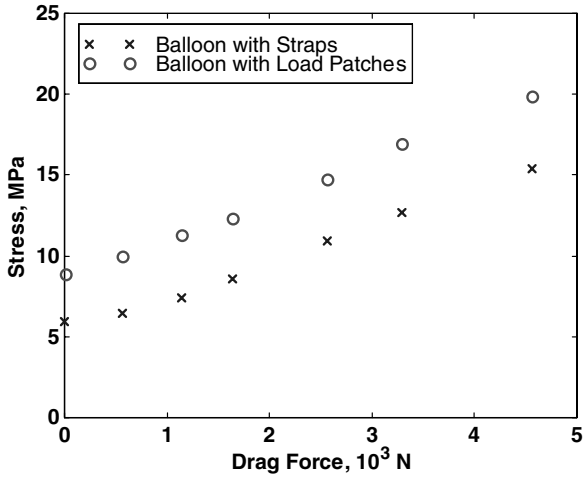

Fig. 12 Maximum stress in aerostats with load patches or straps (1-inWG internal pressure).

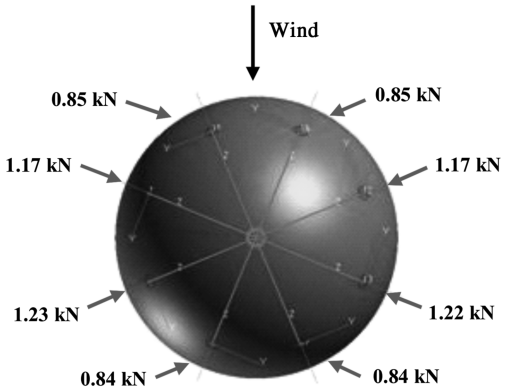

Fig. 13 Constraint force in each tether (bottom view, balloon with load patches).

for tethered buoyant spheres. They found that at a subcritical Reynolds number of 1.40×10^5, the drag coefficient would be around 0.7. Because supercritical drag coefficients tend to be lower than subcritical, the drag coefficient of 0.7 was conservatively used for analysis purposes and design purposes, as described later in Sec. IV.

Figures 10 and 12 show that at higher wind speeds, there is a linear relationship between the drag force and maximum envelope stress where the tethers meet the envelope in both the aerostat with load patches and the aerostat with straps. Because the drag force on a sphere depends proportionately on the drag coefficient, as illustrated by Eq. (1), it follows that the maximum stress in the envelope will also depend proportionately on the drag coefficient. Hence, when considering the more realistic drag coefficient of 0.7, the highest stress in the envelope of the aerostat with load patches in a 20-m/s wind is expected to be 19.9 MPa$(0.7/0.23) = 60.6$ MPa, and the highest stress in the aerostat with straps is expected to be 15.4 MPa$(0.7/0.23) = 46.9$ MPa.

The second idealization in the analysis is that the loads are distributed evenly among the tethers. However, as an aerostat moves through the air, it is common for the tethers to become unevenly loaded. For example, during the experiments in Sec. II, the 2.5-m aerostat occasionally pitched, with one or more of the tethers slackening and then retensioning. Consider a situation in which the simulated aerostat pitches slightly about the confluence point, and the tether in the region of the largest stresses momentarily experiences the entire load while still oriented tangent to the balloon. In this case, the maximum stress experienced by the envelope will rise by eight times, from 60.6 to 485 MPa when load patches are used and from 46.9 to 375 MPa when straps are used.

The factor of 8 assumes that the loads are evenly distributed among the tethers in the models. However, the tethers were not evenly loaded in the simulation, as illustrated by Fig. 13, due to the uneven application of the aerodynamic and internal pressures. On the other hand, the simulation, being static, does not take into account that the tethers can experience dynamic (or shock) loading, which significantly raises the stresses in the envelope. A thorough dynamic analysis of the forces on the balloons is beyond the scope of the present research, and so the factor of 8 was used as a compromise to describe both uneven loading and dynamic effects.

In the case of an aerostat with load patches, the stresses rise to 3.4 times the 142 MPa breaking strength of the 205-g/m^2 envelope laminate when uneven loading and a high drag coefficient are considered, and in the case of an aerostat with straps, the stresses rise to 2.6 times the breaking strength. It follows that the fabric balloons investigated would be incapable of reliably surviving wind speeds even below the dimple speed. Because 20-m/s winds can regularly occur in some environments, it becomes relevant to consider how an aerostat might be redesigned to survive much higher wind speeds.

IV. Partial-Hard Aerostat Design

There are aerostats in existence that can survive winds higher than 20 m/s. A unique example is TCOM's largest, 10, 300-m^3 aerostats, which are designed to survive up to a 46.3-m/s (90-kt) wind [9],

equivalent to a grade-2 hurricane. TCOM achieves this reliability by using very large internal pressures to avoid dimpling, which increase the envelope stresses, and by using heavier materials that can resist these stresses. The present research offers an alternative solution for increasing an aerostat's resistance to point loads in the envelope and dimpling that can be used up to even higher wind speeds, because it does not rely on increasing internal pressure. This is done by reinforcing the envelope using a hard shell in the critical areas of the balloon. Based on Sec. III, these critical areas include the region of tether attachment and the stagnation point, both of which lie approximately on the bottom third of the aerostat for wind speeds above the dimple speed. It was decided to design a 10.15-m-diam spherical partial-hard aerostat that would survive a 46.3-m/s wind with a safety factor of 1.5.

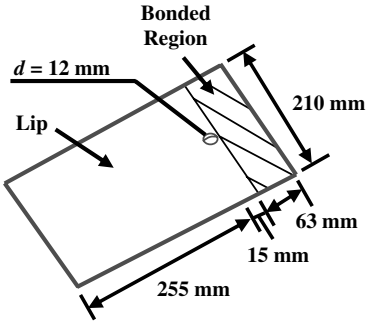

Fig. 14 Tether attachment plate (top view).

A. Designing the Partial-Hard Balloon

Maintaining a low weight (and consequently a high lift) is a critical factor when designing an aerostat. It follows that a hard material with a high strength-to-weight ratio must be used for the shell, such as carbon fiber. Advanced Composites Group's LTM25/CF0511 woven prepreg carbon fiber with the mechanical properties shown in Table 2 was selected for the analysis. Woven carbon fiber was chosen because it can have quasi-isotropic mechanical properties if at least two layers are used with fiber directions oriented at their largest angles from each other [22], and it is less expensive and more readily available than multi-axial carbon fiber. Furthermore, a prepreg was preferred because it ensures that the resin is evenly distributed among the fiber reinforcement, improving strength and reducing the variance in mechanical properties across the composite, and it eases the molding process by allowing for a hand layup [23].

The LTM25 epoxy resin used in the carbon fiber composite is not helium-impermeable, thus requiring a full 10.15-m helium-enclosing envelope to be embedded in the carbon fiber shell. The fabric chosen for the envelope was Lamcotec's 142-g/m^2 (4.2-oz/yd^2) urethane-coated nylon, presented in Sec. II, because it is light and workable.

The tethers were designed to attach to the tangent of the aerostat 35 deg below its equator using mildly curved rectangular plates bonded to the side of the carbon fiber shell. The design of the tether attachment plates was kept simple, because the main interest of the analysis is the protective shell. The plates (Fig. 14) have a bonded region and a protruding lip with a hole lined by a grommet through which the tethers pass. The recommended adhesive for the plates is Loctite's Hysol E-20HP, which has a tensile strength of 39.3 MPa and a shear strength of 28.6 MPa when bonded to epoxy.

The tether attachment plates were designed to withstand the simple loading scenario in which one tether takes the entire load in a 46.3-m/s wind while still coming off the tangent of the balloon. Peel and bending loads were neglected because they are less commonly experienced by an aerostat in flight. Based on a drag coefficient of 0.7 and a factor of safety of 1.5, the expected tether load would be 112 kN, requiring a 12-mm Cortland plasma rope. It was found that to resist the shear and tearing stresses in their lips and the tensile stress concentrations at their holes, the tether attachment plates would have to be made out of 10 layers of carbon fiber and have the dimensions shown in Fig. 14. Further details can be found in [15].

The edges of the adhered region of the tether attachment plates are bonded to the shell 35 deg below the equator of the spherical aerostat. To clear the plates, the carbon fiber shell was brought up to 33 deg below the equator. A fully fabric 10.15-m balloon with a drag coefficient of 0.23 will experience a blowdown angle of 42.5 deg when subjected to the dimpling wind speed of 20 m/s. At this speed, the stagnation point of the wind lies on the carbon fiber shell 42.5 deg $-$33 deg $=$9.5 deg below the fabric–carbon-fiber interface, and so dimpling is prevented. In fact, the extra weight of the partial-hard balloon combined with the higher drag coefficient of a tethered buoyant sphere will result in a steeper blowdown angle, thus moving the stagnation point further toward the bottom of the balloon.

The number of layers needed for the shell was determined iteratively by first predicting the maximum stress that the load-patch-equipped fabric aerostat in Sec. III would see in a 46.3-m/s wind based on the rise in drag force. The number of layers of carbon fiber needed to resist this stress was then calculated, the new aerostat was checked for failure using a finite element model of the partial-hard balloon (described later), and the design was revised as necessary. The best results were found when using two layers of carbon fiber in the shell and a ring of five layers that started 45.2 deg below the equator of the balloon and rose to 33 deg below (Fig. 15), thus encompassing the tether attachment region.

Based on the results in Sec. III, eight 25-mm-wide and 3-mm-thick nylon straps were employed to attach the fabric envelope to the carbon fiber shell, rather than load patches. The straps ran over the top of the balloon and were sewn directly into the envelope. At the end of each strap was a metal ring (see Fig. 1) through which one of the eight tethers passed before going through the hole of a tether attachment plate, as illustrated in Fig. 15. This alleviates some of the load seen by the plates. The fabric envelope was also glued to the carbon fiber along the rim of the shell using an epoxy glue to minimize movement between the two.

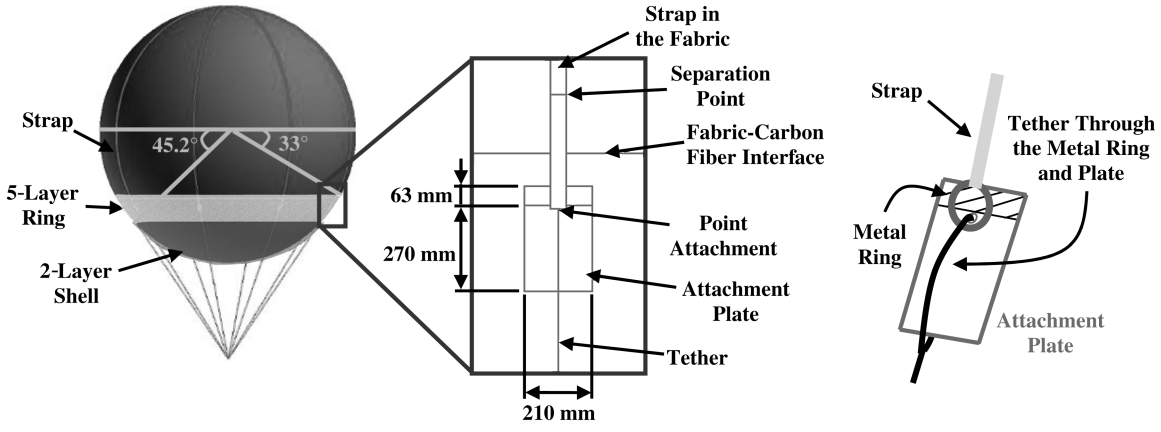

Fig. 15 Simulated carbon fiber shell, straps, and tether attachment plates.

Table 2 Material properties for Advanced Composites Group's LTM25/CF0511 carbon fiber

Fiber direction modulus	65.6 GPa	Compression strength	405 MPa
Shear modulus	3.17 GPa	Shear strength	78.2 MPa
Poisson's ratio	0.03	Areal density	435 g/m^2
Tensile strength	562 MPa	Per-layer thickness	0.28 mm

B. Finite Element Model

In the absence of detailed matrix and fiber information, the LTM25/CF0511 carbon fiber was modeled as being linear elastic isotropic with the mechanical properties shown in Table 2. This was deemed acceptable because, as stated already, when using more than one layer of the woven prepreg, it is expected to have quasi-isotropic properties. The number of layers of the composite used was described in the model by the thickness of the carbon fiber in multiples of the single-layer thickness, thus assuming a perfect bond between the sheets.

The carbon fiber shell was created as a semispherical section covering the bottom of a theoretical sphere of 10.15 m in diameter, starting 33 deg below its equator. Eight tethers emanated from the tangent of the shell 35 deg below the equator of the sphere. The tethers were modeled identically to those in Sec. III, save that their diameter was increased to 12 mm to accommodate the higher loads in the present model. The end node of each tether was tied to a node on the lip just below the edge of the adhered region of a tether attachment plate to approximate the attachment interface. The carbon fiber shell and tether attachment plates were all made out of triangular shell elements, with approximately 5000 mesh elements in total used for all carbon fiber parts of the partial-hard balloon.

The helium-enclosing fabric envelope was modeled similarly to the strap-equipped 10.15-m aerostat in Sec. III. The glued region was approximated by tying nodes around the rim of the carbon fiber shell to the fabric envelope. The straps separated from the envelope 1 deg above the fabric–carbon-fiber interface and ran to the tether attachment point on the lips of the attachment plates. One node on the end of each strap was tied to both the lip and the end of each tether. The material for the fabric balloon was assumed to be linear elastic isotropic nylon 6 with a thickness of 0.15 mm and an areal density of 142 g/m^2. Approximately 17,000 mesh elements were used for the fabric envelope of the partial-hard balloon.

The simulated loads and constraints for the partial-hard model were similar to those of the fabric model in Sec. III. The aerodynamic pressure was applied only to exposed surfaces and not to protected areas such as the fabric enclosed within the carbon fiber shell. The internal pressure profile described by Eq. (2) was applied only to the fabric sphere and straps. The tethers were constrained from translating in any direction, identically to the model in Sec. III.

C. Results of the Finite Element Analysis

The hoop stress in the fabric envelope at the point that is diametrically opposite the stagnation point on the partial-hard aerostat was analytically calculated with Eq. (3) to be 7.98 MPa in a 46.3-m/s wind. The hoop stress returned by NASTRAN at that point was within 1.5% of the expected value, validating the model. Similar results were found for both the hoop stresses and tether constraint forces over all the wind speeds simulated.

The relationship between the drag force on the aerostat and the stress concentrations where the straps separate from the fabric sphere around the tether attachment plates in the carbon fiber shell and the maximum membrane stresses of the fabric envelope are shown in Fig. 16 for several different wind speeds from 0 to 46.3 m/s. In all cases, the stress rose linearly with a rise in drag force, and the stress in the carbon fiber shell was lowest, because it is thicker than the fabric envelope. The stress profiles over the fabric envelope of the partial-hard aerostat for wind speeds of 0, 20, and 46.3 m/s are shown in Fig. 17. The section of the envelope protected by the carbon fiber shell is easily discerned as semispheres of low stress in the plots. Figures 16 and 17 show that the straps holding the fabric sphere to the carbon fiber shell saw lower stresses compared with the envelope around it, similar to the strap-equipped fully fabric balloon in Sec. III. In general, the stress profile over the unprotected section of the fabric envelope for all wind speeds emulated the static pressure distribution on the sphere, with the magnitude of stress increasing as the wind speeds rose.

A more detailed plot of the stresses in the fabric envelope of the partial-hard aerostat for the design wind speed of 46.3 m/s is shown in Fig. 18. The highest stress in the envelope equals 45.5 MPa. This is

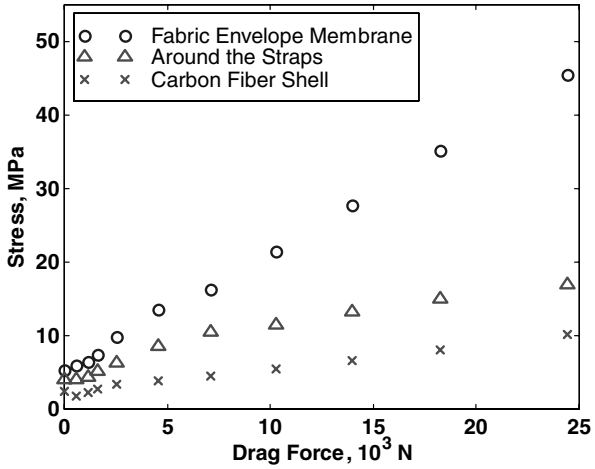

Fig. 16 Maximum stresses in different sections of the partial-hard aerostat.

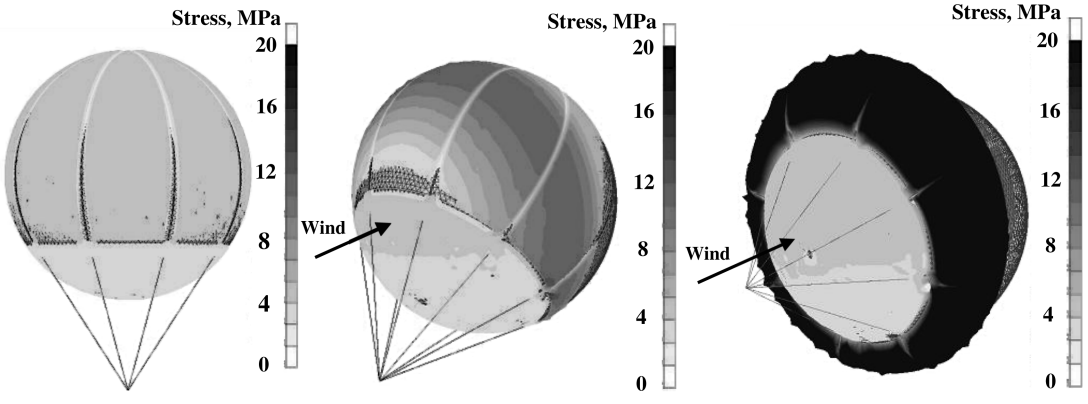

a) 0 m/s **b) 20 m/s** **c) 46.3 m/s (design speed)**

Fig. 17 Stress profiles over the fabric envelope of the partial-hard aerostat subjected to different wind speeds (exaggerated displacements, range narrowed to 0–20 MPa for all plots).

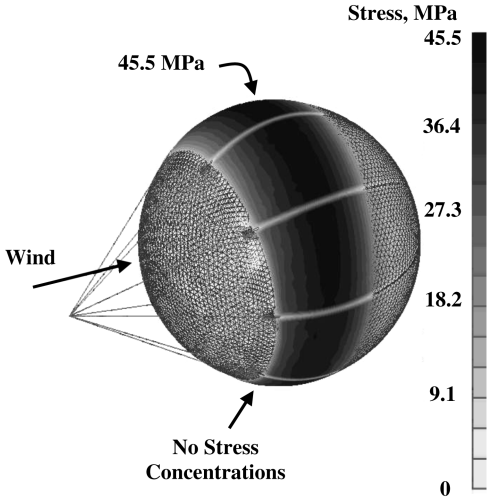

Fig. 18 Stress in the fabric envelope in a 46.3-m/s wind (unexaggerated displacements).

exclusively a membrane stress, which can be calculated using Eq. (3), and is caused by the combination of internal and external pressures at that point in the envelope. Consequently, this stress occurs at the top of the balloon, approximately 80 deg back from the stagnation point, where the largest negative aerodynamic pressure combines with the largest internal pressure. The simulation was run assuming a low drag coefficient of 0.23 over the sphere. Following the logic in Sec. III, a more realistic drag coefficient of 0.7 should be used. It is speculated that this maximum stress will not rise much with a rise in drag coefficient from 0.23 to 0.7. If we consider Fig. 6, we find that the ideal zero-drag (potential flow) case for a smooth fixed sphere has a static pressure distribution that is symmetrical from the front to the back of the sphere. Any nonideality, such as friction, will tend to reduce the flow velocity over the front half, thus reducing the magnitude of the negative peak pressure reached when $\phi = 90$ deg. Based on this, it is expected that a higher drag coefficient would not lead to a larger negative peak pressure coefficient. Rather, the mechanism for a larger drag coefficient is more likely exemplified by the one curve in the plot at a subcritical Reynolds number of 1.62×10^5, for which we see a larger negative low-pressure region on the rear half of the sphere, but with a lower peak negative pressure coefficient.

The negative aerodynamic pressure over the back of the fabric sphere will try to suck it out of the carbon fiber shell, loading the straps. The stress depicted in Fig. 18, however, does not appear to concentrate where the straps separate from the envelope. The reason for this is that the glued area alleviates some of the tension in the straps and ensures that they are evenly loaded, resulting in a maximum stress of just 17 MPa in that region. The stress around the strap separation points is different from the membrane stress discussed previously, in that the contributing factors to the stresses in the former are not the aerodynamic and internal pressures at those points in the envelope, but rather the net aerodynamic suction on the envelope, which loads the straps and is associated with the distribution of negative pressures on the rearward part of the sphere. Hence, it is expected that this stress *will* rise linearly with a rise in drag coefficient. If one were to take into account the more realistic drag coefficient for a tethered buoyant sphere of 0.7, rather than the value of 0.23 assumed for the simulation, the maximum stress of 17 MPa rises to 51.7 MPa. Considering the 152 MPa breaking strength of the 142-g/m^2 Lamcotec fabric in the weaker weft direction, there is a safety factor of 2.9 in the fabric envelope.

Figure 19 shows the stresses in the carbon fiber shell of the partial-hard balloon for wind speeds of 0, 20, and 46.3 m/s. Unlike the fully fabric balloon, because the carbon fiber shell is not flexible and because there is no internal pressure on it, the stagnation point is clearly visible, and we can see that this point is contained within the carbon fiber shell for wind speeds above the dimple speed of 20 m/s.

Overall, the stresses in the carbon fiber shell are highest around the tether attachment plates and the stagnation point. There were also relatively high stresses, up to 8 MPa in a 46.3-m/s wind, at the rim of the shell where the fabric sphere came in contact with the carbon fiber. The stresses at the rim are caused by several factors. As mentioned previously, the glued area around the rim bears some of the load that would ordinarily be experienced by the straps. Moreover, the fabric envelope expanded and pressed against the shell at higher wind speeds. An allowance could be made to account for this stretching, but the balloon only bulges about 50 mm beyond the carbon fiber shell in a 46.3-m/s wind, and the slight contact pressure aids the glue in fixing the two together. Finally, the difference in elastic properties between the fabric and carbon fiber would have contributed to the stress at the rim, where the two materials were joined.

A more detailed plot of the stresses in the carbon fiber shell for a 46.3-m/s wind can be seen in Fig. 20. At this speed, the stresses on the bottom of the shell were 2–3 MPa larger than at the top, a consequence of the buoyant fabric sphere pulling upward on the carbon fiber shell through the straps. The highest stresses in the carbon fiber section in the 46.3-m/s wind were from 6.5 MPa up to 10.2 MPa and occurred in the regions around and below the tether attachment plates and behind the lips of the plates. These stresses derive from the carbon fiber shell tugging on the tethers, due to the net drag on the system. Figure 16 shows that this stress exhibits a linear relationship with drag force and hence with the drag coefficient. If the more realistic drag coefficient of 0.7 for a tethered buoyant sphere is taken into account, and if one tether coming off the tangent of the shell briefly undertakes the entire load, the maximum stress of 10.2 MPa rises to $(10.2\ \text{MPa})(0.7/0.23)(8) = 248$ MPa.

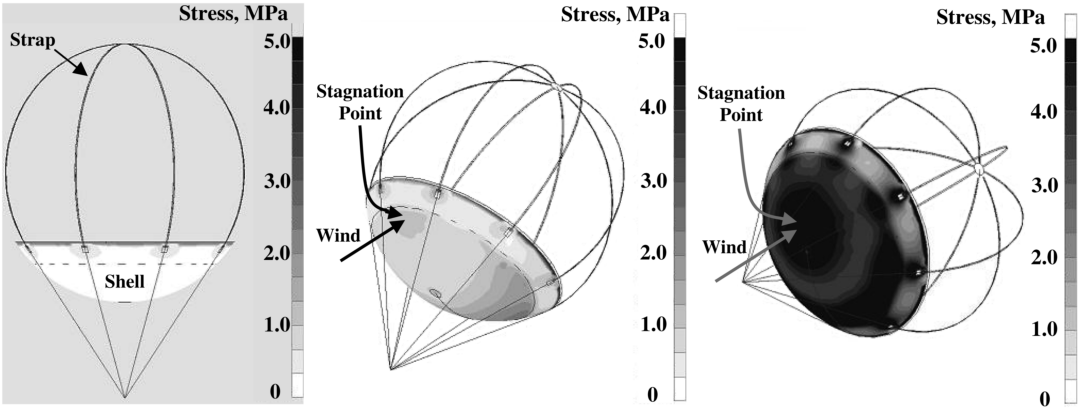

a) 0 m/s **b) 20 m/s** **c) 46.3 m/s (design speed)**

Fig. 19 Stress profiles over the carbon fiber shell of the partial-hard aerostat subjected to different wind speeds (unexaggerated displacements, range narrowed to 0–5 MPa for all plots).

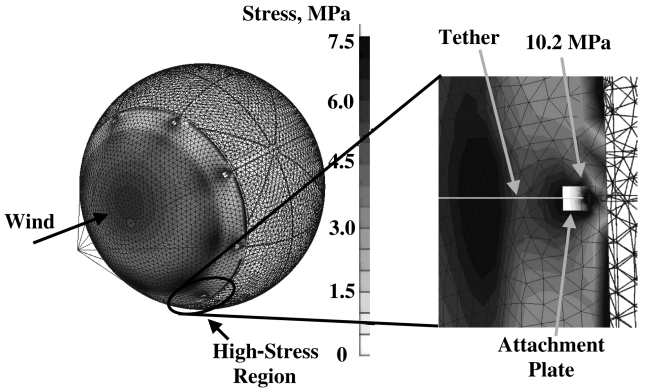

Fig. 20 Stress in the carbon fiber shell in a 46.3-m/s wind (unexaggerated displacements).

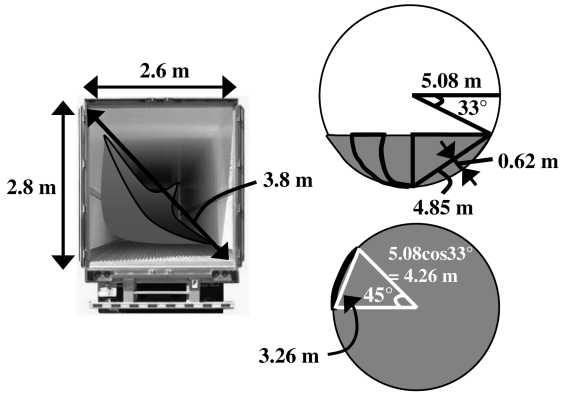

Fig. 21 Fitting the shell into a standard semitrailer.

The resulting safety factor is 1.6 when considering the carbon fiber's 405 MPa compressive strength, above the target value of 1.5.

D. Practical Considerations

The envelope and shell of the partial-hard aerostat presented weigh 165 kg together, whereas the envelope of a conventional 10.15-m-diam spherical balloon only weighs 79.5 kg. To compensate for the extra weight, the diameter of the partial-hard aerostat would have to be increased to approximately 11.75 m. If an increase in diameter of this magnitude is not acceptable, the weight of the partial-hard balloon could be reduced by using a lightweight 85-g/m^2 urethane bladder for the protected bottom third of the fabric balloon. Furthermore, those sections of the carbon fiber shell that see low stresses and do not risk being exposed to the stagnation pressure in wind speeds above the dimple speed can be removed. Using these two strategies would cut the weight difference by more than a third.

There are large ovens and autoclaves that can accommodate curing the hard shell of the 10.15-m partial-hard balloon in one piece. However, making the shell in one piece would then require a means to transport that piece to the launch site. A more practical solution is to make the carbon fiber shell out of eight cylindrical gores that would fit into a standard 14.6 m (48 ft) long by 2.6 m (102 in.) wide by 2.8 m (100 in.) tall semitruck trailer (Fig. 21), and then assemble it by adhesive bonding onsite. The use of eight cylindrical gores is beneficial because it allows the load from each tether to be taken by a solid piece of carbon fiber. Another solution would be to lay the carbon fiber in its mold and cure it at a moderate temperature in a heated hangar on site, allowing the strength of a single-piece shell to be retained.

V. Conclusions

The design of a robust helium aerostat began with the construction of a 2.5-m-diam spherical balloon to review conventional design and construction methods. It was found that although building an aerostat in-house is three to five times cheaper than buying one off the shelf, construction time is lengthy, the potential for error is large, and the final result is of poorer quality. This led us to conclude that the purchase of experimental balloons from a professional supplier would be warranted for future research. The 2.5-m aerostat was flown outdoors while moored to the ground by a single tether to observe its operational characteristics.

Finite element analyses of the stresses in the envelopes of two 10.15-m-diam spherical fabric aerostats in a 20-m/s wind detected the onset of dimple and illustrated that stress concentrations exist at the envelope–tether interface. Using straps instead of load patches to attach the tethers slightly alleviated these stresses, but the concentrations were not eliminated because of the inability of the straps to move relative to the envelope. Moreover, the analysis showed that the aerostat would fail regardless of the tether attachment method used when uneven loading among the eight tethers was considered.

A hard shell was designed to protect the bottom third of a 10.15-m-diam spherical aerostat so that it could survive a 46.3-m/s (90-kt) wind. In the high wind, the fabric envelope saw relatively low stresses, yielding a safety factor of 2.9. With a shell on the bottom third of the aerostat, the stagnation point was contained within the carbon fiber regions for wind speeds above the dimple speed. Using a two-layer carbon fiber shell with a ring of five layers around the tether attachment points, a general safety factor of 1.6 was attained for the balloon. The weight of the aerostat was doubled for the ultrarobust aerostat design, but considering that there is not a comparably sized balloon that can survive 46.3-m/s winds, the cost incurred may be deemed acceptable.

The accuracy of the finite element models was checked using hand calculations of the expected hoop stresses in the balloon and constraint forces in the tethers. Moreover, the stress and displacement profiles around areas such as the stagnation point corresponded to qualitative expectations. However, the analysis performed was limited by the approximations made. For future analyses, it is critical that better approximations for the drag-causing aerodynamic pressure profiles on the aerostat in flight, before and after dimpling, are investigated. These approximations must account for the high drag coefficient of tethered free spheres compared with fixed spheres and the balloon's change in shape under aerodynamic loads. Additionally, a more thorough analysis of the effects of dynamic tether loading on the envelope stresses, either through experimentation or simulation, should be performed. More detailed orthotropic mechanical properties for the simulated material should also be determined, rather than assuming isotropy. Finally, the merits of using a partial-hard envelope on a streamlined aerostat should be investigated.

Acknowledgments

The funding for this project was provided by the Natural Sciences and Engineering Research Council of Canada. We would also like to acknowledge L. Lessard, P. Hubert, I. Sharf, and J. Nemes of McGill University and P. Dewdney of the National Research Council of Canada for their technical suggestions and discussions.

References

[1] Nahum, H., and Marom, S., "Defense and Procurement in Sweden—Aerostat-Borne Systems for Defense and Homeland Security," *Military Technology*, Vol. 26, No. 8, 2002, pp. 102–107.

[2] Khoury, G. A., and Gillett, J. D., *Airship Technology*, Cambridge Aerospace Series 10, Cambridge Univ. Press, Cambridge, England, U.K., 1999.

[3] Upson, R. H., *Free and Captive Balloons*, Ronald Press, New York, 1926.

[4] Recks, R. J., *A Practical Guide to Building Small Gas Blimps*, Recks Publications, Chula Vista, CA, 1997.

[5] Recks, R. J., *An Introduction to Muscle Powered Ultra-Light Gas Blimps*, Recks Publications, Chula Vista, CA, 1998

[6] Williamson, C. H. K., and Govardhan, R., "Dynamics and Forcing of a Tethered Sphere in a Fluid Flow," *Journal of Fluids and Structures*, Vol. 11, Apr. 1997, pp. 293–305.

[7] Govardhan, R., and Williamson, C. H. K., "Vortex-Induced Motions of a Tethered Sphere," *Journal of Wind Engineering and Industrial Aerodynamics*, Vol. 69, July 1997, pp. 375–385.
[8] Govardhan, R., and Williamson, C. H. K., "Vortex-Induced Vibrations of a Sphere," *Journal of Fluid Mechanics*, Vol. 531, May 2005, pp. 11–47.
[9] Hunt, J. D., "Structural Analysis of Aerostat Flexible Structure by the Finite-Element Method," *Journal of Aircraft*, Vol. 19, No. 8, 1982, pp. 674–678.
[10] Hunt, J. D., "Structural Analysis of the Light Weight Hard Nose on the 71M Aerostat," AIAA Paper 93-4037, Sept. 1993.
[11] Baginski, F., and Collier, W., "Modeling the Shapes of Constrained Partially Inflated High-Altitude Balloons," *AIAA Journal*, Vol. 39, No. 9, 2001, pp. 1662–1672.
[12] Baginski, F., and Schur, W., "Structural Analysis of Pneumatic Envelopes: Variational Formulation and Optimization-Based Solution Process," *AIAA Journal*, Vol. 41, No. 2, 2003, pp. 304–311.
[13] Durney, G. P., "Concepts for Prevention of Catastrophic Failure in Large Aerostats," *Global Technology 2000*, AIAA, Reston, VA, 1980, pp. 1–6.
[14] Smalley, J. H., "Development of the e-Balloon," National Center for Atmospheric Research, TR AFCRL-70-0543, Boulder, CO, 1970.
[15] Miller, J., "The Design of Robust Helium Aerostats," M.Eng. in mechanical engineering Thesis, Dept. of Mechanical Engineering, McGill Univ., Montreal, QC, Canada, 2005.
[16] White, F. M., *Fluid Mechanics*, 4th ed., WCB/McGraw Hill, Boston, 1999, pp. 427–492.
[17] Cook, R. D., Malkus, D. S., Plesha, M. E., and Witt, R. J., *Concepts and Applications of Finite Element Analysis*, 4th ed., Wiley, New York, 2002, pp. 595–638.
[18] Lambert, C., "Dynamics Modeling and Conceptual Design of a Multi-Tethered Aerostat System," M.A.Sc. in mechanical engineering Thesis, Dept. of Mechanical Engineering, Univ. of Victoria, Victoria, BC, Canada, 2002.
[19] Harper, C. A., *Modern Plastics Handbook*, McGraw–Hill, New York, 2000.
[20] Moaveni, S., *Finite Element Analysis, Theory and Application with ANSYS*, 2nd ed., Pearsons Education, Upper Saddle River, NJ, 2003, pp. 308–344.
[21] Achenbach, E., "Experiments on the Flow Past Spheres at Very High Reynolds Numbers," *Journal of Fluid Mechanics*, Vol. 54, No. 3, 1972, pp. 565–575.
[22] Weeton, J. W., Peters, D. M., and Thomas, K. L., *Engineer's Guide to Composite Materials*, American Society for Metals, Metals Park, OH, 1987, pp. 1–14.
[23] "Plastic Matrix Composites with Continuous Fiber Reinforcement," *Military Handbook*, U.S. Department of Defense, MIL-HDBK-754 (AR), 1991.